AN INVESTIGATION INTO THE STATIC PERFORMANCE OF THE CALIFORNIA SEA LION FOREFLIPPER

Megan C. Leftwich, Ian Moss, Kartik Bulusu and Aditya Kulkarni
Department of Mechanical and Aerospace Engineering
George Washington University
3000 Science
Engineering Hall, Washington, DC 20052, USA
mleftwich@gwu.edu

Frank Fish
Department of Biology
West Chester University
West Chester, PA 19383, USA
FFish@wcupa.edu

ABSTRACT

The California sea lion (*Zalophus californianus*) produces thrust with its foreflippers when swimming. Sea lions adduct their foreflippers against the body, creating propulsive bursts that are well suited for hunting in the littoral zone. While these bursts have been studied kinematically, it has also been noted through observations that sea lions use their foreflippers statically, like fixed airplane wings, to generate torques needed for extremely agile maneuvers. A mechanical portrait of these morphological functions—and their connections to how evolutionary changes have resulted in an idealized airfoil structure for the flipper—remains incomplete. We find that a static model of a foreflipper performs remarkably like an optimized fixed airplane wing, despite having no obvious primary propulsive purpose. Here we show aerodynamic forces and surface flow streamlines generated by the flipper, while acting as a fixed wing. The flipper takes advantage of three-dimensional flow and known vortical structures commonly found on swept wings for lift generation. We found that the static flipper produces lift over a wide range of angle of attack, including a net-negative angle. Unlike leading-edge structures found in other aquatic mammals, the trailing edge geometry does not delay stall and has no effect in a static sense. Our results demonstrate that to accomplish both fast, forward swimming and highly agile maneuvers, California sea lions use their foreflippers to produce force in two distinct modes: unsteady abduction to produce forward thrust, and the newly discovered steady, fixed wing to produce a rolling torque around their center of mass for maneuvering.

INTRODUCTION

The California sea lion (*Zalophus californianus*) swims through the water by moving its large, protracted foreflippers from above its head into a position abducted against its abdomen (Friedman & Leftwich, 2014). This is different from most high-performance aquatic mammals (dolphins (Rohr *et al.*, 1998; Fish & Rohr, 1999), humpback whales (Fish & Battle, 1995)) and fish (tuna (Anderson & Chhabra, 2002) and sharks (Oeffner & Lauder, 2012)) that generate thrust by moving their fluke or caudal fin—their posterior appendages. There is a large body of work on this type of unsteady, body caudal fin (BCF) propulsion. While this paper cannot offer a comprehensive literature review of the propulsive forces of swimming, reviews are offered by Sfakiotakis, et al. Sfakiotakis *et al.* (1999) and Smits Smits (2019).

Sea lions typically produce thrust by using their foreflippers in a motion called a 'clap'—quickly moving them as a pair from above their head into their abdomen. This causes a jet of fluid to move in one direction, and the sea lion to move in the other, a principle consistent with the conservation of momentum. The process is detailed in Godfrey (1985), Feldkamp (1987*a*,*b*) and Friedman & Leftwich (2014). Following this motion, the animal glides through the water with its foreflippers pressed tightly against its abdomen, minimizing drag during the recovery phase, until it either changes direction or initiates another clap to accelerate further.

This maneuver is executed through the precise coordination of the animal's foreflippers and body segments. The sea lion's propulsive stroke cycle consists of three phases: recovery, power, and paddle, as described in Drago et al. (2024) Drago *et al.* (2024). In the recovery phase, the foreflippers aligns with the flow and extend laterally to minimize drag. The power phase involves pulling the flippers beneath the body while orienting them toward the direction of movement. Finally, in the paddle phase, the flippers align with the motion before settling streamlined alongside the body.

During continuous, straight swimming, sea lions oscillate their foreflippers to propel themselves forward without the assistance of collapsed hind flippers, which trail passively. In maneuvers such as turning and leaping (porpoising), the hind flippers spread into a delta-wing configuration Leahy & F. E. Fish (2021). It is rare for the foreflippers to be extended into the water as the animal moves forward (like the pectoral flippers of the humpback whale or bottle nose dolphin, for example (Fish & Rohr, 1999)). However, the shape of the sea lion foreflipper strongly resembles the fixed wing of an airplane (figure 1a), despite not generating thrust in the same

Figure 1: (*a*) An excised right foreflipper of a deceased adult female California sea lion that shows the ventral side. The smooth edge (left) is the leading edge of the flipper, while the crenelated side (right) is the trailing edge. (*b*) A sea lion completes a banked turn by using the lift generated from the foreflippers operating in a static manner. (Credit - Mark Harris)

manner.

In addition to their unique thrust production, sea lions are also highly maneuverable and flexible aquatic mammals. Maneuverability is crucial to the performance of fast-swimming marine mammals that employ rapid turns to capture prey. Overhead video recordings of sea lions turning in the horizontal plane revealed that unpowered turns were executed through body flexion along with the use of the pectoral and pelvic flippers, which acted as control surfaces Fish *et al.* (2003). They are capable of creating complex shapes with their bodies, including touching their hindflippers to their nose by bending both backwards and forward. In addition, their spines are flexible not only front-to-back but also side-to-side. This flexibility makes sea lions highly maneuverable while navigating the water (Godfrey, 1985; Fish *et al.*, 2003). This maneuverability is desirable for hunting prey and navigating kelp forests or other complex aquatic environments (Fiscus & Baines, 1966); however, it requires that the animal produce forces in addition to simple forward thrust. One way that sea lions do this is by producing a lift force with one extended foreflipper to cause a torque about the animal's center of mass (see Fig. 1b).

California sea lions have the longest foreflipper of any pinniped relative to their bodylength (BL) with its length varying from 27% to 34% of the total BL. Such unusually long propulsive surfaces have been linked to being responsible for increased maneuverability in animals (Fish & Battle, 1995; Edel & Winn, 1978). Furthermore, the cross-sections of the foreflippers strongly resembles the shape of a cambered airfoil (see Fig. 2(a)). This shape is not beneficial for the thrust-producing clap motion. However, is needed for the forces needed to complete the complex maneuvers described above.

In this paper, we investigate the foreflipper's performance as a 'wing' by looking at flow separation as a function of angle of attack as well as the coefficients of lift and drag. We further investigate the effect of the trailing edge structure in the fixed wing-like mode by testing an anatomically correct flipper model and an altered model—with the trailing edge smoothed with an ellipse. Furthermore, we compare our results to the well-studied humpback whale flipper (Miklosovic *et al.*, 2004; Aftab *et al.*, 2016), which operates in a fixed method. This paper will explore their ability to produce the forces needed to create complex underwater maneuvers.

EXPERIMENTAL METHODS

Foreflipper models

The models tested are derived from high-resolution laser scanning (Friedman *et al.*, 2015) of the right foreflipper of a deceased adult California sea lion female (see Fig. 2(a)). Two models were tested: an anatomical model that retains the geometry of the scanned flipper, and a smooth model. The smooth model is a modification of the anatomical model. For this model, the trailing edge is smoothed by choosing an elliptical curve that gives the best approximation of an ellipsoid planform (see Fig. 2(b))). The anatomical and smooth models are scaled to 65% of the full-size flipper but maintain geometric similarity everywhere. The flippers are printed in Acrylonitrile butadiene styrene (ABS) using Stratasys Fortus 250mc (Stratasys, Eden Prairie, MN). The models are sanded down extensively using sandpaper (from 200 to 2000 grit) to remove striations formed during the additive manufacturing process. Thin coats of black primer and paint are applied to the model to remove any remaining surface imperfections. The flipper has a natural twist to it, as seen in Fig.. 2(a), lower panel. The average angle of attack over the entire span of the flipper is zero.

Wind tunnel experiments

Aerodynamic measurements and surface flow visualization are carried out in a low speed, open return wind tunnel with a 9:5:1 contraction ratio, where the flow is generated by a five blade fan that can operate safely at a rate of 2300 rpm. The test section has observation windows on either side and is 0.6 m long, 0.3 m wide and 0.3 m high. The wind tunnel can operate up to air speeds of 65 m/s with a turbulence intensity of less than 0.2%. Force measurements are conducted over five Reynolds numbers between $Re_1 = 60,000$ and $Re_2 = 148,000$ based on the incoming velocity, U, mean chord length, c, and the kinematic viscosity, ν. This range is dynamically similar to a California sea lion swimming at speeds of 0.4 and 1 BL/s, respectively (where 1 $BL = 1.88$ m, is the body length of the sea lion from which the foreflipper was extracted). Lift force, L, drag force, D, and pitching moment, M, are measured simultaneously using a three-axis force sensor (Aerolab three component pyramidal balance) mounted below the test section and connected to the flipper model through a sting apparatus.

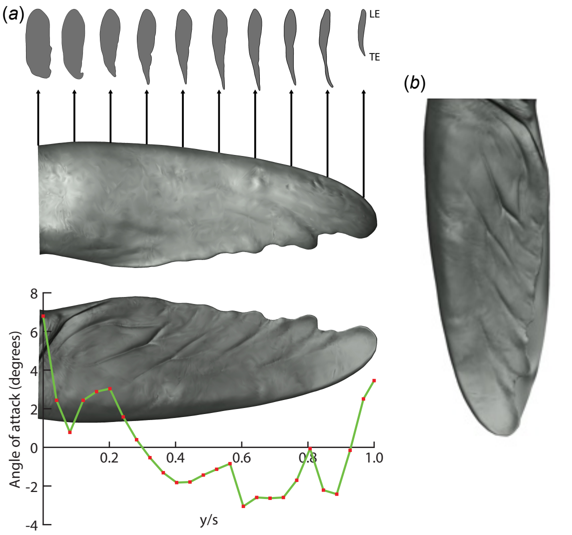

Figure 2: Foreflipper models. (*a*) Closeup of the dorsal and ventral side of the foreflipper along with variation in cross-sections and angle of attack across the span. (*b*) Modified smooth foreflipper.

All force measurements are time-averaged over a sufficient duration to ensure statistical convergence of the results.

Surface oil flow visualization (SOFV) is carried out by coating the suction surface of the foreflipper model with a mixture of finely powdered pigment and an oil medium. This technique, extensively described by Maltby & Keating (1962), involves coating the surface of the object with a thin film of oil which develops a streaky pattern when a fluid flows past the object, carrying the oil with it. For the black paint coated 3D printed sea lion flipper, a mixture of titanium oxide, kerosene and oleic acid (used as an anti-coagulant) is mixed in the ratio of 5:8:1. After a running time of 5 minutes, the low viscosity oil evaporates and leaves behind a detailed pattern that can be analyzed for features such as transition from laminar to turbulent flow, flow separation, and reattachment. The brighter regions on the foreflipper denote areas of low shear stress where the fluid becomes trapped near the surface. Low viscosity oils such as kerosene, light diesel oil, and light transformer oil are recommended for use in low wind speed tunnel testing (Merzkirch, 1987), as they respond well to the relatively weak aerodynamic forces present at low flow speeds. The choice of pigment depends on the contrast provided against the background, with common options including titanium dioxide, ground chalk powder on a dark surface, or lampblack on a white surface. The addition of oleic acid, an anti-coagulant, prevents the pigment from forming lumps and controls the extent of flocculation. The mixture is perfected through trial and error until the streaks form a contrasting and detailed pattern, and is then applied uniformly on the suction side of the flipper using a foam brush.

Four tests are conducted on the anatomical flipper model at $Re_2 = 148{,}000$ at angles of attack of α = -8 °, 0°, 16° and 20°. The model is removed from the test section after each run to photograph the resulting surface oil flow patterns. Three trials are conducted at each angle of attack to verify repeatability, and the results are confirmed to be consistent across all trials. The wind tunnel is operated at $Re_2 = 148{,}000$ based on the mean chord length of the foreflipper for all visualization runs.

Particle Image Velocimetry (PIV) is used to investigate the flow field around the anatomical foreflipper at $Re_1 = 60{,}000$. The flipper is mounted vertically in the test section (2.44 m × 0.91 m × 0.36 m) of an open-end wind tunnel. The tunnel is seeded with a rocket fogger (LaVision UK, Ltd) that releases fog based on a combination of water and glycerin with an aerodynamic diameter of $0.2-0.3\ \mu$. A Litron PIV 50-50 laser (Litron Lasers, Warwickshire, England) is projected through internal optics to create a horizontal light sheet oriented perpendicular to the semi-span of the flipper. The laser sheet illuminates tracer particles within the flow, enabling the velocity field to be reconstructed from successive image pairs captured at short time intervals. For details on the wind tunnel and PIV setup, the reader is referred to Parker & Leftwich (2016).

Four horizontal planes located at 20%, 40%, 60% and 80% of the semi-span are imaged near the suction side of the flipper using an Imager sCMOS camera (LaVision UK, Ltd) at angles of attack of α = -6°, 0°, 4°, 10° and 20°. Measurements very close to the surface of the flipper are difficult to obtain due to bright reflections arising from the complex curvature of the three-dimensional geometry over the span. To overcome these issues, the model is first coated with black paint and then with an in-house fluorescent paint, consisting of a mixture of Rhodamine B, ethanol, and transparent acrylic paint, to attenuate reflections from the surface. Rhodamine B has a strong absorption band near the wavelength of the laser, while its emission occurs in the red wavelength regime. This characteristic optical property of Rhodamine B, coupled with a 532 nm bandpass filter placed in front of the camera, allows the imaging system to effectively filter out orange and red-light reflections originating from the model surface. Since the absorption efficiency of Rhodamine B degrades with repeated exposure to the laser, a thin layer of Dykem Steel Red layout fluid is reapplied to the surface as needed between runs. The combined use of Rhodamine (Paterna *et al.*, 2013) and Dykem (Perce & Lu, 2011) to attenuate near-surface reflection intensities has been well documented individually in the literature, but their application together on the same model as a complementary combination has not previously been reported. It was found that applying a thin coat of Dykem between runs on the Rhodamine-coated model helps preserve the absorption qualities of the fluorescent mixture over the course of the experiment.

RESULTS AND DISCUSSION

Force measurements

The aerodynamic performance along with the efficiency curves of the anatomical foreflipper model (see figure 4a-c) indicate strong aerodynamic performance and trends similar to that of conventional airfoils and wings as predicted by fixed wing theory (Anderson Jr, 1991). At all Reynolds numbers, the anatomical flipper stalls at a relatively high angle of attack, $\alpha = 16°$, with a maximum lift coefficient ($C_L = L/\frac{1}{2}\rho U^2 A$ where L is the measured lift force in Newtons, and A is the projected area of the suction side of the flipper model), $C_{L_{max}} = 1.215 \pm 0.007$ occurring at the highest Reynolds number, Re_2. The value of C_L increases with increasing Reynolds number for each angle of attack. However, the highest three Reynolds numbers tested are nearly identical, and it is assumed that there is no significant Reynolds number dependence above $Re = 100{,}000$, which is equivalent to a swimming speed of 0.681 BL/s (see figure **??**a). A reverse trend is found for the drag coefficient, $C_D = D/\frac{1}{2}\rho U^2 A$ where D is the measured drag force in Newtons, except that at lower angles of attack,

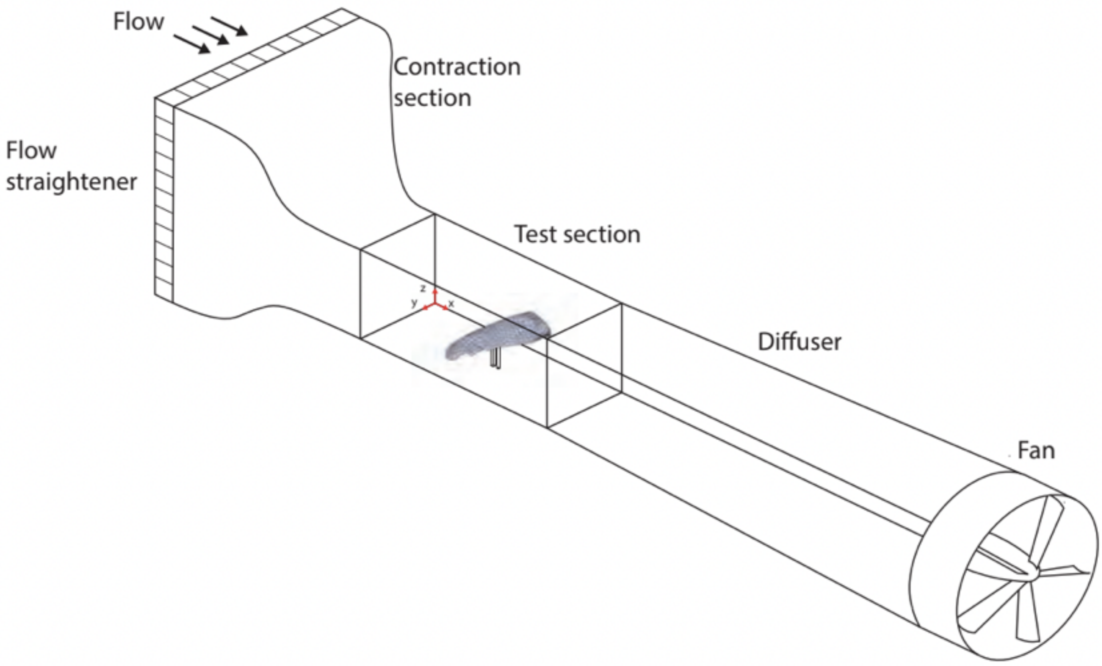

Figure 3: The flipper models are mounted low speed open return wind tunnel with a 9:5:1 contraction ratio.

there is a greater dependence on Reynolds number on C_D (see figure 4b).

Figure 4c shows the aerodynamic efficiency of the anatomical flipper model, where increasing aerodynamic efficiency is observed with increasing Reynolds number, although, as expected, the dependence weakens at higher Reynolds numbers. The flipper model has an aspect ratio (AR = Semi-Span/Projected flipper area) of 3.1, which is relatively high compared to many biological propulsive surfaces. This high aspect ratio plays an important role in the overall aerodynamic performance of the flipper, as it serves to minimize induced drag, which is produced as a consequence of lift generation by a finite wing. As a result, the flipper achieves an improved lift-to-drag (L/D) ratio compared to lower aspect ratio propulsive surfaces (Anderson Jr, 1991), suggesting that the high aspect ratio foreflipper geometry of the California sea lion is well adapted for efficient hydrodynamic force generation during swimming.

Figures 4d-f show the same data as figures 4a-c, but for the smoothed flipper model (see figure 2b). The curves are very similar to those for the anatomical flipper. Note that for all curves in figures 4a-f, errors are shown in the shaded area around the data line. The bottom row panels for figure 4 shows the difference in C_L (g), C_D (h) and L/D (i) between the anatomical model and the smooth model ($\Delta C_L = C_{L,anatomical} - C_{L,smooth}$, $\Delta C_D = C_{D,anatomical} - C_{D,smooth}$, and $\Delta L/D = L/D_{anatomical} - L/D_{smooth}$). ΔC_L and ΔC_D have values very close to zero for the entire measurement space. There is not a significant different in ΔC_L with the smooth flipper producing slightly more lift than the anatomical flipper. For the ΔC_D case, the anatomical flipper produces less drag than the smooth flipper from around -4° to stall at the lowest Reynolds number and from 8° to stall at the highest Reynolds number tested. This is evident in the lift over drag ratio (figure 4i) where the performance of the anatomical flipper is on par with or slightly better at high α while the smooth flipper has a considerably better performance at low to moderately high α (note that the scale is an order of magnitude larger for $\Delta L/D$ than ΔC_L and ΔC_D). Thus, while the trailing edge crenulations do not help in delaying stall (as in the case of the leading edge tubercles of humpback flippers (Fish & Battle, 1995)), the flipper geometry for the sea lion as a whole exhibits good aerodynamic performance.

Contrary to studies suggesting that the angle of attack of propulsive surfaces should be small to avoid separation of flow and eventually stall for mammals using lift-based propulsion(Fish, 2001), we find that these flippers produce positive lift over a wide range of angles of attack before encountering a gradual stall around α as high as 16°. This gradual stall behavior, rather than an abrupt loss of lift, suggests that the complex three-dimensional geometry of the foreflipper may play a role in delaying flow separation and extending the effective operating range of the flipper. In addition, while exhibiting the behavior of a fixed wing at moderate to high Reynolds numbers, the flipper also produces positive lift at significantly negative angles of attack, from α as low as -5°, due to the overall effect of camber on the incoming flow. This ability to generate lift across such a broad range of angles of attack highlights the aerodynamic versatility of the California sea lion foreflipper as a propulsive surface.

Fish & Lauder (2017) suggest that the propulsive surfaces of most aquatic vertebrates are nearly symmetric in cross section. Earlier studies by Feldkamp (1987*a*), Fish (2004) and Castellini & Mellish (2015) did not have the benefit of three-dimensional laser scanning and concluded that the cross-sections of the sea lion foreflipper were symmetric. However, high-resolution scans of the flipper reveal that the cross sections strongly resemble cambered airfoils (figure 2a). These cambered airfoil cross-sections, with a maximum camber ranging from 2-9%, indicate evolutionary favoritism towards passively producing lift as a default mechanism, even in the absence of active muscular control. Figure 2a also shows

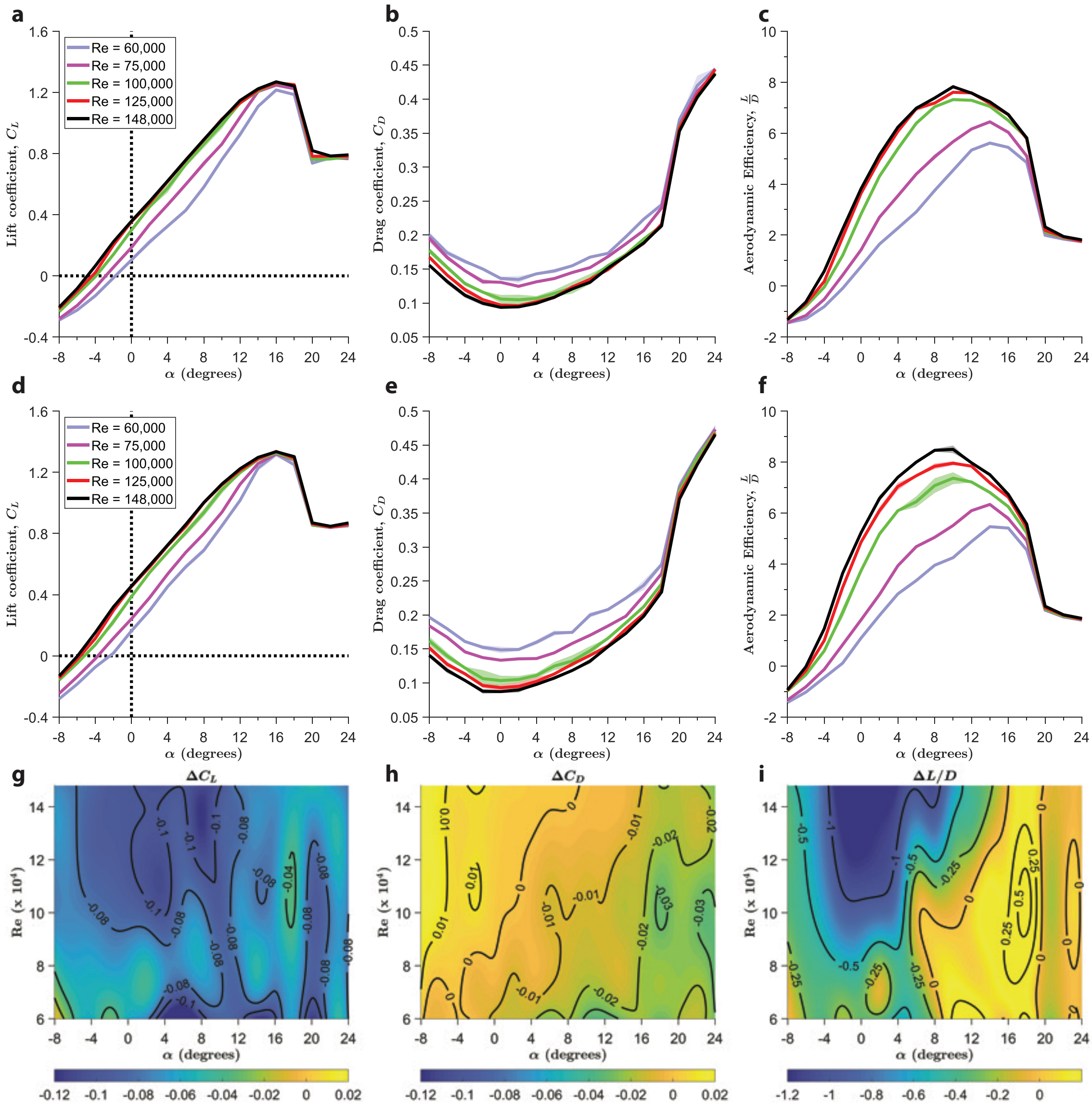

Figure 4: Aerodynamic forces (C_L, C_D, $\frac{L}{D}$) generated on the anatomical (*a-c*) and smooth flipper (*d-f*). Difference in lift coefficient (*g*), drag coefficient (*h*), and aerodynamic efficiency (*i*) between the anatomical trailing edge flipper and the smooth trailing edge flipper where $\Delta C_L, \Delta C_D, \Delta\frac{L}{D} = (\Delta C_L, \Delta C_D, \Delta\frac{L}{D})_{anatomical} - (\Delta C_L, \Delta C_D, \Delta\frac{L}{D})_{smooth}$

the variable change in the local angle of attack for the different cross-sections of the flipper, which decreases progressively from root to tip. This geometric twist allows the root to stall before the tip, thereby avoiding instability in roll during maneuvering. When coupled with the aerodynamic twist stemming from the variable change in thickness and camber along the span, the overall flipper geometry promotes an optimal elliptical lift distribution (Fish & Battle, 1995; Hurt, 1965). Such a distribution is considered aerodynamically ideal, as it minimizes induced drag while maximizing lift generation efficiency across the entire span of the foreflipper.

It appears that sea lions are capable of exploiting this lift performance to complete their characteristic high angle banked turns, which require them to produce enough force to generate the required centripetal acceleration. The ability of the foreflipper to generate high lift explains how sea lions can produce accelerations of up to 5 g's and turning rates of 690°/s during rapid maneuvers (Fish *et al.*, 2003). As the flippers are located near the sea lion's center of gravity, they bring about a controlled instability that the sea lion can exploit to be highly maneuverable by using only one flipper to complete an unpowered turn (figure. 1b). The maneuvering capabilities of the sea lion are possible because of its lift generation that is the result of the cambered profile of the flipper coupled with low sweep and a high aspect ratio.

Surface oil flow visualization

We use surface oil flow visualization (SOFV) to investigate the boundary layer attachment and vortical structures associated with the high lift generation of the foreflipper. SOFV at $Re_2 = 148,000$ revealed spanwise flow and vortex dominated regions over the suction surface of the foreflipper (see Fig. 5). The applied oil conforms to the direction of the local air flow due to the shear at the air/oil interface, indicating the wall streamlines and regions of separation-reattachment and vortices (Merzkirch, 1987). At negative and zero α (Fig.5a and b), the flow is attached over most of the flipper with the

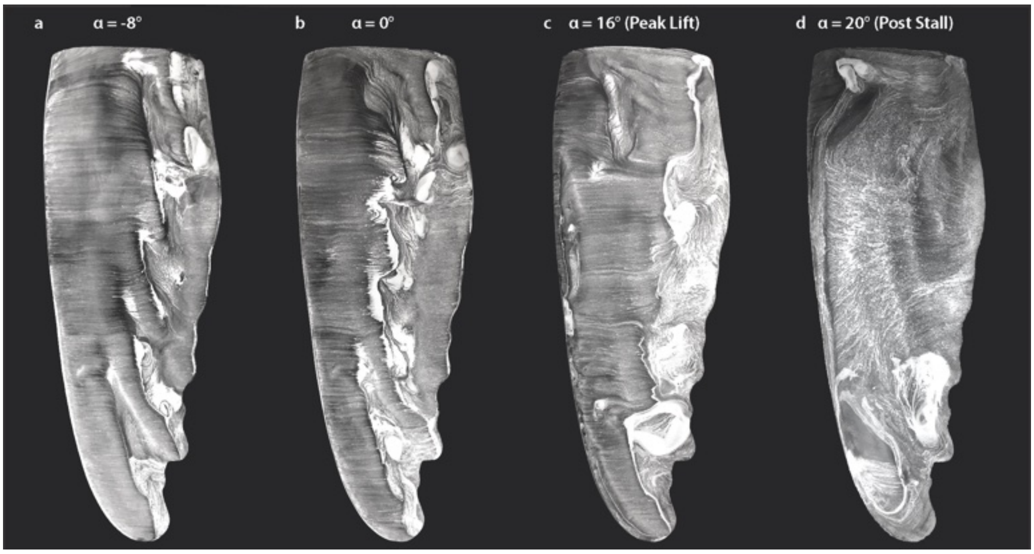

Figure 5: Surface streamlines on the dorsal side of the foreflipper at $Re = 148,000$. *(a-d)*, Surface oil flow visualization conducted on the anatomical foreflipper using titanium oxide and kerosene at α (*a*) $-8°$, (*b*) $0°$, (*c*) $16°$ and (*d*) $20°$.

presence of short separation bubbles near the mid-chord after which the flow again reattaches. Near the root, the streamlines converge and turn inwards towards the flipper with substantial crossflow.

At peak lift, which occurs at $\alpha = 16°$ just before stall, the attached flow quickly separates to form a short separation bubble near the tip, with spanwise flow from the leading edge feeding the tip vortex (Fig. 5c). Also noticeable is a foci near the trailing edge that denotes the presence of a counter-rotating vortex. Stall occurs when the flow separates close to the leading edge with a vortex situated at the leading edge (Fig. 5d). The spanwise flow over the foreflipper is driven by the troughs that run spanwise turning outward towards the trailing edge and variation in geometric and aerodynamic twist (See Fig. 2 in the Methods section). This is analogous to surface contouring as described by Werle *et al.* (1987) where ripples or creases are used for stall alleviation to yield maximum lift at high lift conditions.

At $\alpha = 20°$ which is the post-stall regime, there is reverse flow almost entirely over the surface of the flipper. The flow separates at the leading edge and does not reattach again. Additionally, a vortex can be seen very close to the leading edge at the tip. SOFV reveals that the flow over the flipper is highly three-dimensional in nature and also dominated by spanwise flow. The troughs and crests seem to play a major role in deciding the location of the short separation bubbles and the limiting streamlines.

Flowfields

Normalized streamwise velocity, U_x/U_∞, at Re_1 are shown in figure 6 over a range of spanwise positions on the suction (dorsal) side of the anatomical foreflipper. Each row represents a different spanwise location (from top row to bottom row the spanwise locations are 80% span, 60% span, 40% span and 20% span). Each column represents the ensemble-averaged, streamwise flow (from left to right) over the flipper at a specific angle of attack ($-6°$, $0°$, $4°$, $10°$, and $14°$). Although the SOFV was conducted at Re_2, it can be seen that the flow in the spanwise direction over the flipper varies considerably due to the variation in geometric and aerodynamic twist along the span. Comparing each column (flow over a constant α) reveals notable differences in flow structures, as well as the location of attachment and reattachment of separation bubbles across the span. For $\alpha = -6°$ (see Fig. 6, leftmost column), as we move from the root of the flipper towards the tip, flow separation is observed over the entire suction surface. At this angle of attack, the flipper produces negative lift as shown in figure 4a, consistent with the dominance of separated flow across the span. As the angle of attack is increased up to $14°$, there is a progressive reduction in the extent of flow separation. At $\alpha = 4°$, the presence of small laminar separation bubbles can be identified along all spanwise positions except at 20% span, where complete separation of flow persists. These small separation bubbles are observed recurring at multiple spanwise locations and at different angles of attack, most notably at $\alpha = 14°$ near the tip of the flipper.

At $\alpha = 14°$, the flow appears to be completely attached over the majority of the flipper surface, representing the condition of peak aerodynamic efficiency prior to stall onset. Beyond this angle of attack, separated flow begins to dominate progressively across the entire flipper surface until full stall is reached at $\alpha = 16°$. This gradual progression of separation from root to tip is consistent with the geometric twist of the flipper, which is designed to ensure that the root stalls before the tip, thereby preserving roll stability during maneuvering. The PIV data presented here captures the complex spanwise variation in flow structures, and when considered alongside the qualitative whole-surface view provided by the SOFV results (see Fig. 5), offers a comprehensive picture of the three-dimensionality of the flow field around the foreflipper across the range of angles of attack tested.

CONCLUSIONS

The primary mechanism of sea lion locomotion is to use their foreflippers in a hydrodynamically active way by means of the 'clap' to produce thrust. However, the results presented here show another way that sea lions use their foreflippers in a hydrodynamically passive way. While propelling forward, the sea lion abducts one (or both) of its flippers and extends it laterally to produce the necessary lift—and torque—required for agile and small radii turns. This passive usage of its propulsive surfaces has never been documented or studied in pinnipeds,

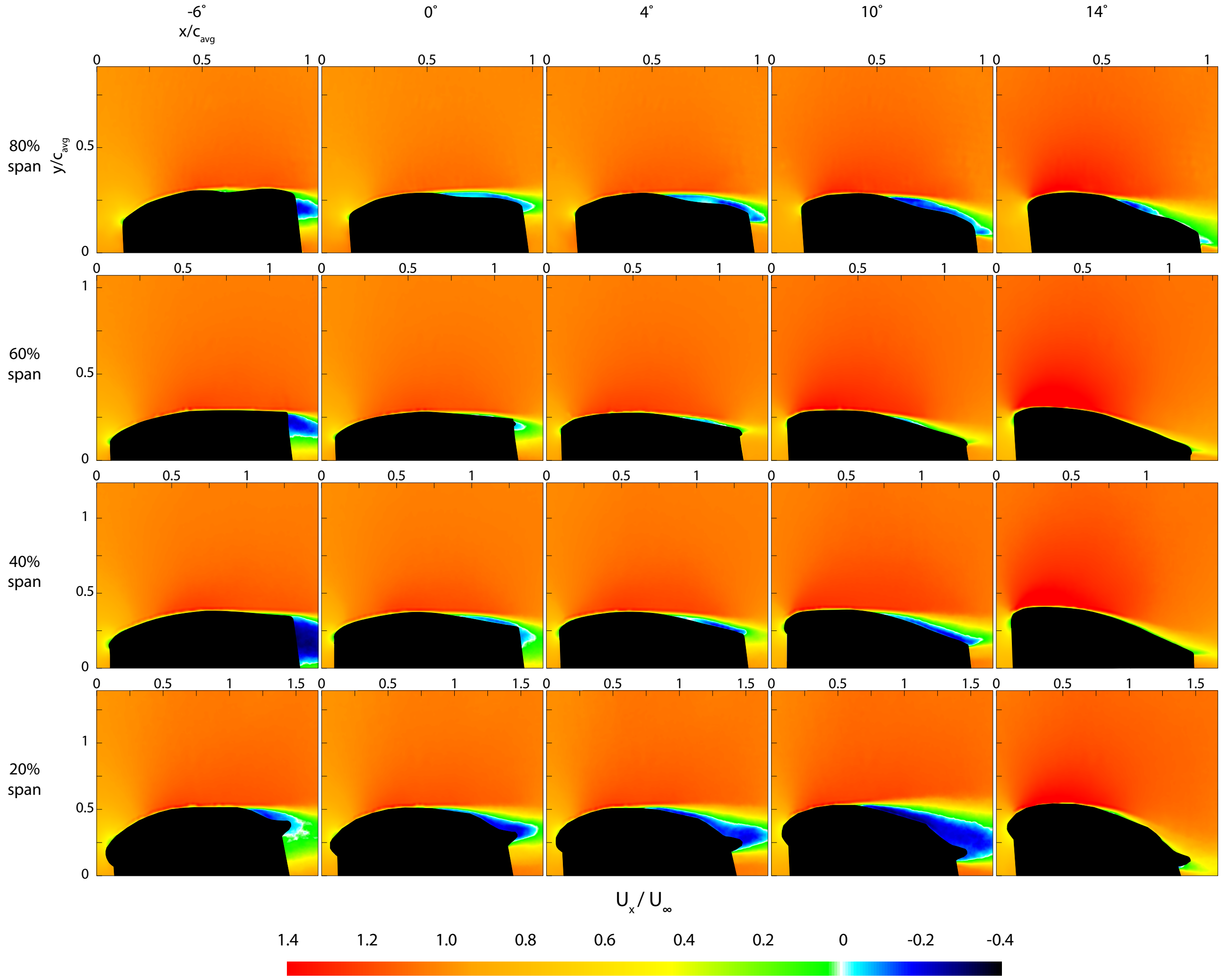

Figure 6: Near surface streamwise velocity over the anatomical foreflipper. The rows of the matrix relate to spanwise positions from the root (0% span) of the flipper, while the columns are the average angle of attack of the flipper, α, at which data was taken.

but greatly contributes to their ability to maneuver in complex underwater environments. The broad range of angles of attack over which the foreflipper generates positive lift, combined with its gradual stall characteristics, suggests that the sea lion is capable of producing maneuvering forces across a wide variety of swimming speeds and body orientations without the risk of abrupt loss of hydrodynamic control.

The cambered cross-sectional geometry of the foreflipper, previously overlooked in earlier studies that lacked the benefit of high-resolution three-dimensional scanning, indicates that the flipper is passively optimized to generate lift even at zero angle of attack, further enhancing its utility as a maneuvering surface. The aerodynamic and geometric twist of the foreflipper, which promotes an elliptical lift distribution and delays tip stall, further underscores the sophistication of this dual-purpose propulsive surface. The high aspect ratio of the foreflipper minimizes induced drag during lift-based maneuvering, while the spanwise variation in camber and thickness ensures that lift is generated efficiently across the entire span. Together, these morphological features reflect a remarkable degree of evolutionary optimization, enabling the foreflipper to serve simultaneously as a thrust-producing and maneuver-controlling appendage across a wide range of swimming conditions.

Sea lions have thus evolved a single propulsive surface, their foreflipper, that produces forces using two distinct fluid mechanics principles. Thrust is produced through a clapping motion that creates a jet of fluid against the direction of travel (see Fig. 7a); and maneuvering forces (torques) are produced using a lift-based method of force generation (see Fig. 7b). The lift performance attributes of the foreflipper provide the sea lion with enhanced maneuverability and thrust production as an aquatic predator navigating the complex and dynamic habitats of the marine environment. These findings have broader implications for the bio-inspired design of underwater vehicles, where the integration of a single multifunctional control surface capable of both thrust generation and maneuvering force production could offer significant advantages in terms of simplicity, efficiency, and agility. Future studies examining the active muscular control of the foreflipper during free-swimming maneuvers, combined with the passive hydrodynamic properties documented here, will be essential to fully characterize the role of the foreflipper in sea lion locomotion and to further inform the development of next-generation bio-inspired aquatic propulsion systems.

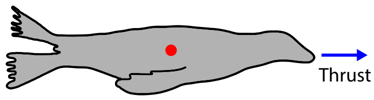

(a) Clapping mechanism

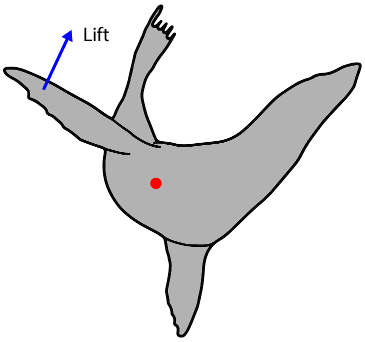

(b) Lift generation mechanism

Figure 7: (*a*) Primary mechanism of thrust production in an hydrodynamically active way — clap. (*b*) Secondary mechanism of force production by using one of the flippers as a lifting wing to generate a torque for turning.

REFERENCES

Aftab, SMA, Razak, NA, Rafie, AS Mohd & Ahmad, KA 2016 Mimicking the humpback whale: An aerodynamic perspective. *Progress in Aerospace Sciences* **84**, 48–69.

Anderson, Jamie M & Chhabra, Narender K 2002 Maneuvering and stability performance of a robotic tuna. *Integrative and Comparative Biology* **42** (1), 118–126.

Anderson Jr, John D 1991 *Fundamentals of Aerodynamics, McGraw-Hill*.

Castellini, Michael A & Mellish, Jo-Ann 2015 *Marine mammal physiology: Requisites for ocean living*. CRC Press.

Drago, A., Kadapa, S., Marcouiller, N., Kwatny, H. G. & Tangorra, J. L. 2024 Using reinforcement learning to develop a novel gait for a bio-robotic california sea lion. *Biomimetics* **9**, 522.

Edel, RK & Winn, HE 1978 Observations on underwater locomotion and flipper movement of the humpback whale megaptera novaeangliae. *Marine Biology* **48** (3), 279–287.

Feldkamp, Steven D 1987*a* Foreflipper propulsion in the california sea lion, zalophus californianus. *Journal of Zoology* **212** (1), 43–57.

Feldkamp, Steven D. 1987*b* Swimming in the california sea lion: Morphometrics, drag and energetics. *Journal of Experimental Biology* **131**, 117–135.

Fiscus, Clifford H & Baines, Gary A 1966 Food and feeding behavior of steller and california sea lions. *Journal of mammalogy* **47** (2), 195–200.

Fish, FE 2001 A mechanism for evolutionary transition in swimming mode by mammals. *Secondary Adaptation of Tetrapods to Life in Water. Verlag Dr. Friedrich Pfeil, München* pp. 261–287.

Fish, Frank E 2004 Structure and mechanics of nonpiscine control surfaces. *IEEE Journal of Oceanic Engineering* **29** (3), 605–621.

Fish, Frank E & Battle, Juliann M 1995 Hydrodynamic design of the humpback whale flipper. *Journal of Morphology* **225** (1), 51–60.

Fish, Frank E., Hurley, J. & Costa, Daniel P. 2003 Maneuverability by the sea lion zalophus californianus: turning performance of an unstable body design. *Journal of Experimental Biology* **206** (4), 667–674.

Fish, Frank E & Lauder, George V 2017 Control surfaces of aquatic vertebrates: active and passive design and function. *Journal of Experimental Biology* **220** (23), 4351–4363.

Fish, Frank E & Rohr, JJ 1999 Review of dolphin hydrodynamics and swimming performance. *Tech. Rep.*.

Friedman, Chen, Joel, Bryan W, Schult, Allen R & Leftwich, Megan C 2015 Noninvasive 3d geometry extraction of a sea lion foreflipper. *Journal of Aero Aqua Bio-Mechanisms* **4** (1), 25–31.

Friedman, C & Leftwich, MC 2014 The kinematics of the california sea lion foreflipper during forward swimming. *Bioinspiration & biomimetics* **9** (4), 046010.

Godfrey, Steven J 1985 Additional observations of subaqueous locomotion in the california sea lion (zalophus californianus). *Aqu. Mamm* **11**, 53–57.

Hurt, Hugh H 1965 *Aerodynamics for naval aviators*. Office of the Chief of Naval Operations, Aviation Training Division.

Leahy, A. M. & F. E. Fish, S. J. Kerr, J. A. Zeligs S. Skrovan K. L. Cardenas 2021 The role of california sea lion (*Zalophus californianus*) hindflippers as aquatic control surfaces for maneuverability. *J. Exp. Biol.* **224**.

Maltby, RL & Keating, RFA 1962 The surface oil flow technique for use in low speed wind tunnels. *Flow Visualization in Wind Tunnels Using Indicators, RL Maltby, compiler, AGARDograph* **70**, 29–38.

Merzkirch, Wolfgang 1987 *Flow visualization*, 2nd edn. Academic Press inc.

Miklosovic, DS, Murray, MM, Howle, LE & Fish, FE 2004 Leading-edge tubercles delay stall on humpback whale (megaptera novaeangliae) flippers. *Physics of fluids* **16** (5), L39–L42.

Oeffner, Johannes & Lauder, George V 2012 The hydrodynamic function of shark skin and two biomimetic applications. *Journal of Experimental Biology* **215** (5), 785–795.

Parker, Colin M & Leftwich, Megan C 2016 The effect of tip speed ratio on a vertical axis wind turbine at high reynolds numbers. *Experiments in Fluids* **57** (5), 74.

Paterna, Enrico, Moonen, Peter, Dorer, Viktor & Carmeliet, Jan 2013 Mitigation of surface reflection in piv measurements. *Measurement science and technology* **24** (5), 057003.

Perce, Adam & Lu, Frank 2011 New seeding and surface treatment methods for particle image velocimetry. In *49th AIAA aerospace sciences meeting including the new horizons forum and aerospace exposition*, p. 1164.

Rohr, J. J., Hendricks, E. W., Quigley, L., Fish, F. E., Gilpatrick, J. W. & Scardina-Ludwig, J. 1998 Observations of dolphin swimming speed and strouhal number. United States Navy Technical Report 1769.

Sfakiotakis, Michael, Lane, David M & Davies, J Bruce C 1999 Review of fish swimming modes for aquatic locomotion. *IEEE Journal of oceanic engineering* **24** (2), 237–252.

Smits, Alexander J 2019 Undulatory and oscillatory swimming. *Journal of Fluid Mechanics* **874**.

Werle, MJ, Paterson, RW & Resz, WM 1987 Trailing-edge separation/stall alleviation. *AIAA journal* **25** (4), 624–626.